Addition of Ammonium Thiocyanate Alters the Microstructure and Energetic Landscape of 2D/3D Perovskite Films

Duim, Herman; Rommens, Alex J.; Shao, Shuyan; Portale, Giuseppe; Loi, Maria A.

Published in:
ACS Applied Energy Materials

DOI:
10.1021/acsaem.3c00545

Publication date:
2023

ACS APPLIED ENERGY MATERIALS

www.acsaem.org

Forum Article

Addition of Ammonium Thiocyanate Alters the Microstructure and Energetic Landscape of 2D/3D Perovskite Films

Herman Duim, Alex J. Rommens, Shuyan Shao, Giuseppe Portale, and Maria A. Loi*

Cite This: ACS Appl. Energy Mater. 2023, 6, 10285−10293

Read Online

ACCESS | Metrics & More | Article Recommendations | Supporting Information

ABSTRACT: Mixtures of low-dimensional and 3D perovskite phases have attracted significant attention due to their improved stability with respect to purely 3D perovskites. One of the strategies to gain control over the complex crystallization of these 2D/3D perovskite films and obtain well-ordered thin films is through the additive engineering of the precursor solution. In this work, the influence of ammonium thiocyanate addition on the microstructural and optical properties of thin films of $(PEA)_2(MA)_{n-1}Pb_nI_{3n+1}$ is investigated for different n values. Apart from improving the texture of the thin films, it was found that the addition of ammonium thiocyanate also impacts the morphology and energetic landscape in $(PEA)_2(MA)_{n-1}Pb_nI_{3n+1}$.

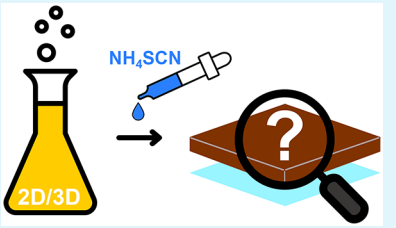

KEYWORDS: *2D/3D perovskite films, solar cells, orientation control, additive engineering, optical properties, microstructure*

INTRODUCTION

Metal halide perovskites are a promising class of materials for their use in a broad range of (opto)electronic applications such as solar cells,[1] light-emitting diodes,[2] photodetectors,[3] X-ray detectors,[4] and even spintronic applications.[5] While record power conversion efficiencies for perovskite-based solar cells have now reached values exceeding 25%,[6] the poor stability of these materials under ambient conditions, heat, and prolonged light exposure still poses a major obstacle for their successful transfer to industry.[7−9] A strategy that is gaining a strong foothold in perovskite literature is the use of low-dimensional perovskite derivatives in order to increase the material's intrinsic stability. In the so-called 2D perovskites, which follow the general formula A_2BX_4, 2D layers of inorganic octahedra (BX_6) are separated by relatively long organic spacers (A), thereby forming a quantum-well-like structure. Compared to their 3D analogues, 2D perovskites have a low enthalpy of formation and are considered to be inherently more stable.[10,11] Their increased environmental stability, however, comes at the cost of increased exciton binding energies[12] and anisotropic charge transport,[13] which limit the applicability of these materials in photovoltaics.

A solution is found in quasi-2D perovskites of the form $A'_2A_{n-1}B_nX_{3n+1}$, in which n denotes the number of inorganic layers (ABX_3) sandwiched between long organic spacer molecules (A′), which provides a compromise between the increased quantum confinement and stability improvement when long organic cations are introduced into the 3D perovskite structure. In practice, however, thin films of quasi-2D perovskites tend to form mixtures of different low-dimensional as well as 3D-like perovskite phases rather than forming a single $A'_2A_{n-1}B_nX_{3n+1}$ phase.[14] Adequate control over the distribution and orientation of quasi-2D phases is key to obtaining high device efficiencies because the presence of too many low n-value phases or an unfavorable alignment of the inorganic layers with respect to the electrodes will impede charge transport through the active layer.[15−17]

Thus far, several methodologies have been proposed to effectively control the phase distribution and orientation of the inorganic slabs within these 2D/3D perovskite films. Tsai et al., for instance, demonstrated that heating of the precursor solution and substrate prior to deposition can induce the preferred vertical alignment in these films.[18,19] Such a hot-casting technique, however, requires the substrate temperature to be raised to a relatively high temperature of 150 °C and is prone to user-dependent variability.

Alternative approaches attempt to obtain orientation control through solution engineering. It was shown that the orientation of $(BA)_2(MA)_3Pb_4I_{13}$ (n = 4; BA = butylammonium; MA = methylammonium) can, for example, be improved when *N*,*N*-dimethylformamide (DMF) is replaced by a binary solvent of DMF and dimethyl sulfoxide, due to the lower evaporation rate of the latter.[16]

In the case of 3D perovskites, the addition of thiocyanates (SCN^-, where ammonium, methylammonium, or lead are commonly used as counterions) can also slow down the crystallization rate, leading to an improvement in the film quality and stability for a range of compositions.[20−28] This approach has recently been extended to the case of 2D/3D

Special Issue: Halide Perovskite Materials and Devices for Energy and Electronic Applications

Received: March 7, 2023
Accepted: August 8, 2023
Published: August 16, 2023

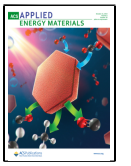

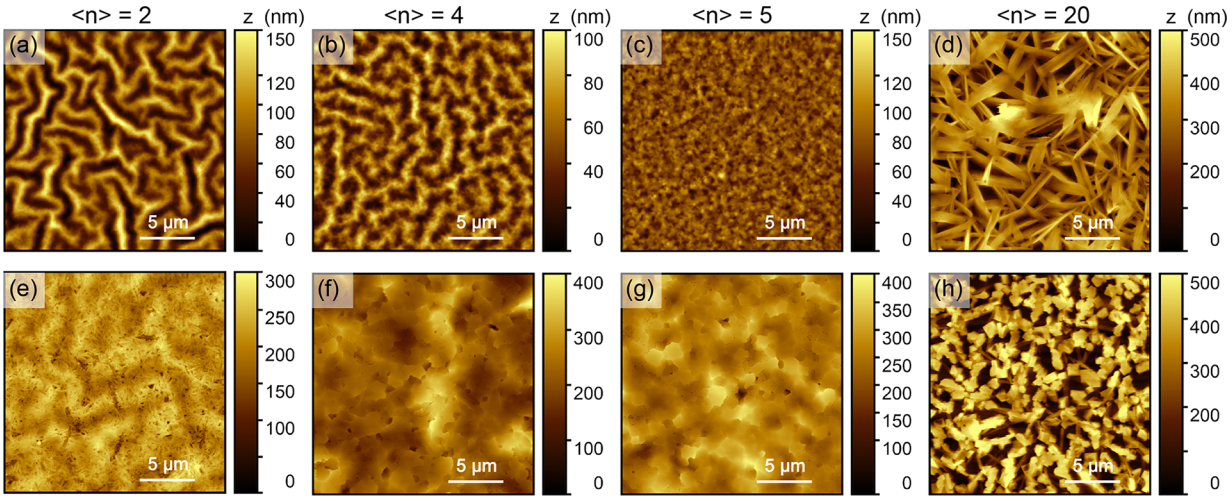

Figure 1. AFM micrographs of the (a–d) pristine and (e–h) NH_4SCN 2D/3D perovskite films for different $\langle n \rangle$ values, showing the effect of both increasing PEA content and the addition of NH_4 on the film morphology. Lateral scales are identical for all images, while the *z*-scale varies per image.

perovskite films, where the addition of NH_4SCN to the precursor solution induces a strong alignment of the inorganic planes perpendicular to the substrate, facilitating charge transport through the active layer and thereby greatly improving the solar cell efficiencies while eliminating the need for hot casting.[29,30]

Similar improvements in the out-of-plane orientation were obtained by Li et al. when thiocyanate was added to a Dion–Jacobson-type 2D/3D perovskite film based on 1,4-butanediammonium, while simultaneously improving the phase purity of the material.[31] Ruggeri et al., on the other hand, reported that, for the case of $(PEA)_2(FA)_2(Pb_{0.5}Sn_{0.5})_3I_{10}$ (PEA = phenethylammonium; FA = formamidinium), the addition of NH_4SCN also leads to an increased ordering of the quasi-2D perovskite phases but with the inorganic layers oriented parallel to the substrate rather than the desired perpendicular orientation.[32] Moreover, the authors found that increasing the concentration of thiocyanate favors the formation of low-*n*-value perovskite phases over the 3D-like perovskite.

While the incorporation of low-dimensional perovskites into a 3D perovskite film can thus instill many of the favorable properties of the 2D perovskites into the hybrid material, obtaining adequate control over the phase distribution and orientation remains challenging. Considering the pronounced impact that the precursor chemistry is expected to have on the final material properties, a more encompassing inquiry is needed to understand the effects of additive engineering on the resulting 2D/3D perovskite films. In this work, we build on the existing body of work on orientation-regulating strategies by carefully assessing the influence of NH_4SCN addition on the microstructural and optical properties of $(PEA)_2(MA)_{n-1}Pb_nI_{3n+1}$ for different nominal *n* values. We assert here that the introduction of NH_4SCN to these 2D/3D perovskite films not only leads to the expected increase in the crystallinity and texture of these materials but also substantially alters their morphology, phase distribution, and, consequently, their energetic landscape. The addition of NH_4SCN favors the formation of low-dimensional perovskite phases at the perovskite/substrate interface, leading to a distinct absorption and radiative recombination from low-*n*-value perovskite phases in 2D/3D perovskite films of up to $n = 20$. At the same time, the 3D-like perovskite phases are found to more closely match the emission of the parent 3D perovskite $MAPbI_3$ than their pristine counterparts, and a fast energy funneling toward these low-band-gap phases is observed. These observations strengthen our understanding of orientation regulation through NH_4SCN addition and highlight the large impact that changes in the crystallization dynamics can have on the energetic landscape of 2D/3D perovskite films.

RESULTS AND DISCUSSION

We cast films of 2D/3D perovskites with a composition of $(PEA)_2(MA)_{n-1}Pb_nI_{3n+1}$ for different ratios of PEA to MA, namely, $\langle n \rangle = 2$, 4, 5, and 20, as well as a 3D $MAPbI_3$ film. Note that the ratios and nominal compositions listed throughout the text refer to the stoichiometry of the precursor solution and do not necessarily reflect the stoichiometry of the phases that are ultimately formed. In order to investigate the impact of SCN^- addition on the phase distribution, orientation, and resulting optical properties of these films with different nominal *n* values, we compare films that are cast from DMF (hereafter referred to as pristine) and DMF + 0.4 M NH_4SCN. This particular concentration of NH_4SCN is based on a recipe that we have previously established for the fabrication of high-efficiency 2D/3D perovskite solar cells.[15] Because $[SCN]^-$ has been reported to act as a pseudohalide and can therefore potentially substitute I^- in the perovskite structure, the samples were annealed at 100 °C for 10 min to evaporate any remaining thiocyanate ions.[24] Fourier transform infrared (FTIR) spectroscopy confirms the absence of vibrational modes originating from $[SCN]^-$ (Figure S1), such that all properties discussed in this work can be attributed to differences in the morphology, phase distribution, and orientation rather than a difference in the chemical composition of the metal halide framework. Whether the source of thiocyanate (e.g., $PbSCN_2$ instead of NH_4SCN) has any impact at all on these properties is subject to further study.

Morphology, Texture, and Phase Distribution. In agreement with previous literature reports, the X-ray diffraction patterns of these films demonstrate a clear improvement in the crystallinity upon the addition of NH_4SCN.[9,28,30] While this holds true for all $\langle n \rangle$ values investigated here, the largest effect

https://doi.org/10.1021/acsaem.3c00545
ACS Appl. Energy Mater. 2023, 6, 10285–10293

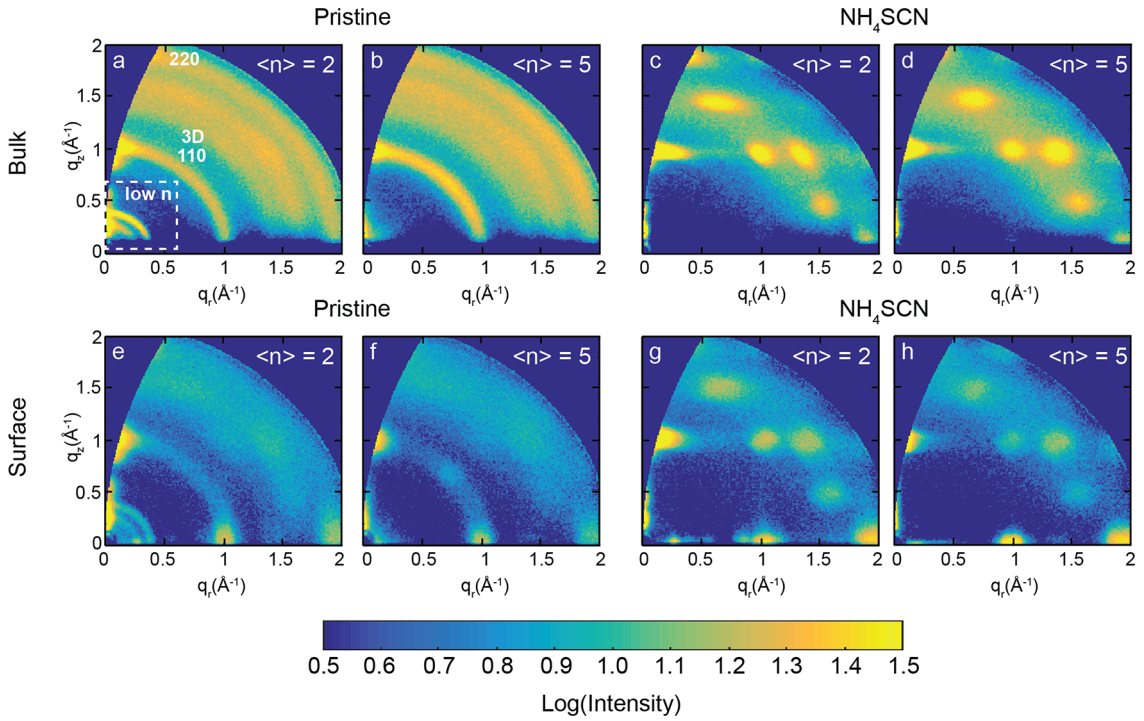

Figure 2. Bulk GIWAXS patterns of the $\langle n \rangle$ = 2 and 5 films for the pristine (a and b) and NH_4SCN (c and d) cases. (e and h) GIWAXS patterns of the same films obtained from the surface layer.

is observed for thin films with a nominal value of $\langle n \rangle$ = 5 (Supplementary note 1 and Figures S2 and S3). In line with this, solar cells fabricated from the $\langle n \rangle$ = 5 films indeed show improved performance upon the addition of NH_4SCN (Figure S4).

The impact that the addition of both PEA^+ and NH_4SCN has on the crystallization dynamics of the perovskite film is also clearly reflected by the differences in their morphologies, as observed from the atomic force microscopy (AFM) images reported in Figure 1. For low n values, the pristine films (Figure 1a–d) possess a wrinkled morphology with a fine-grained substructure superimposed (see Figures S5 and S6 for high-resolution AFM images). As the $\langle n \rangle$ value increases to 5, the wrinkled structure vanishes and a more homogeneous morphology is obtained. When, however, the PEA content is reduced even further to obtain a nominal value of $\langle n \rangle$ = 20, the film exhibits incomplete surface coverage and is composed of large needlelike growth structures that are reminiscent of the uncontrolled crystallization of the $MAPbI_3$ precursor phases (Figure S7).[33] The poor morphology of the 3D perovskite film, in this case, stems from the deposition process being optimized for the deposition of smooth 2D/3D films rather than being optimized for the fabrication of pure 3D films.

The addition of NH_4SCN to the precursor solution drastically altered the observed morphology for all $\langle n \rangle$ values. The large-scale wrinkled structure still persists in the $\langle n \rangle$ = 2 film, while on a smaller scale, a network of platelet-like grains can be resolved. For the $\langle n \rangle$ = 4 and 5 films, individual flat grains with dimensions of up to 1 μm can be resolved clearly, in contrast to the small grains of the pristine films. The increased grain size upon NH_4SCN addition is, however, accompanied by an increased surface roughness (see Table S8 for the root-mean-square values). As in the pristine film, incomplete surface coverage is obtained when the concentration of PEA^+ cations in the precursor solution is no longer sufficient to mediate the crystallization ($\langle n \rangle$ = 20).

To probe the distribution and crystallographic orientation of different perovskite phases throughout the depth of the films, we performed grazing-incidence wide-angle X-ray scattering (GIWAXS) measurements at different angles of incidence. By use of an angle of incidence exceeding the critical angle for total external reflection ($\alpha_i = 1.5° > \alpha_c$), the entire thickness of the film can be probed, whereas at smaller angles ($\alpha_i = 0.25°$), the X-rays only penetrate several tens of nanometers into the film. Figure 2 shows the bulk GIWAXS patterns of the pristine and NH_4SCN $\langle n \rangle$ = 2 and 5 films as exemplary cases (see Figures S9 and S10 for the GIWAXS patterns of all 2D/3D films). Figure S11 shows examples of indexed GIWAXS patterns, while Figure S12 shows the bulk 3D GIWAXS pattern for reference. For the pristine films, the (110) planes of the 3D phase exhibit a diffraction arc with a weak preferential orientation along q_z. A large scattering intensity from the (00n) planes of low-n-value phases can be observed at small q values (dashed box), particularly for the $\langle n \rangle$ = 2 film. Despite the tendency of these low-n-value perovskite phases to align with their inorganic slabs parallel to the underlying substrate,[34] a random orientation for some of the low-n-value phases can, nonetheless, be observed in the pristine $\langle n \rangle$ = 2 film, marking the particularly uncontrolled crystallization of this film.

In keeping with previous reports, the addition of NH_4SCN introduces strong alignment of the (110) planes of the 3D-like phases parallel to the substrate; i.e., their inorganic planes are oriented perpendicular to the substrate, as evidenced by the appearance of a Bragg spot along q_z in Figure 2c,d. It is interesting to note here that when the nominal n value is further increased to $\langle n \rangle$ = 20, the difference between the pristine and NH_4SCN films is minimal (Figure S9), indicating that the mechanism of orientation control through NH_4SCN addition does not work well for large $\langle n \rangle$-value perovskites.

https://doi.org/10.1021/acsaem.3c00545
ACS Appl. Energy Mater. 2023, 6, 10285−10293

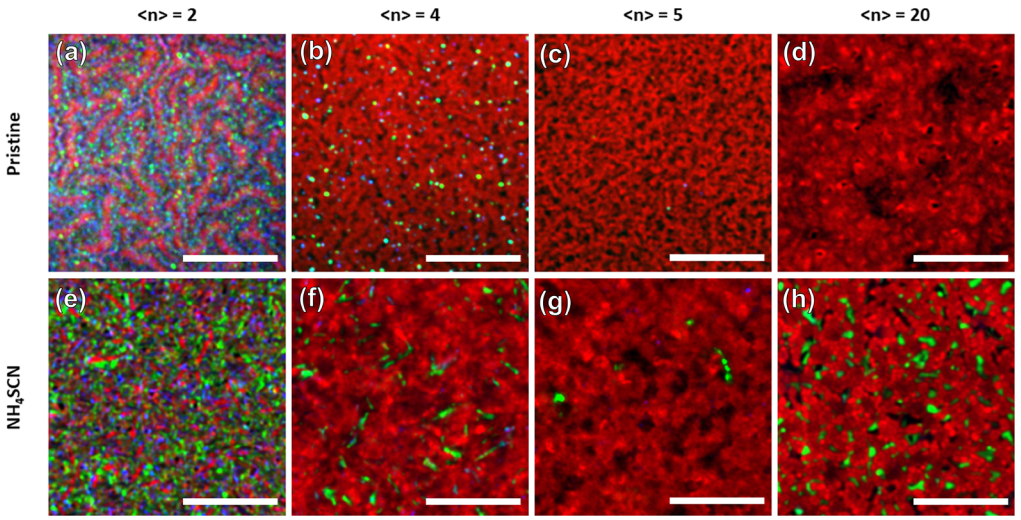

Figure 3. PL maps of the (a–d) pristine and (e–h) NH_4SCN 2D/3D films acquired by CLSM using three different detection channels. The red channel is sensitive to photon energies below 1.91 eV, corresponding to emission from the 3D-like perovskite phases, the green channel corresponds to $n = 2$ and 3 phases that emit in the range of 1.94–2.30 eV, and finally the blue channel detects photons in the energy range of 2.28–2.56 eV, capturing the emission from $n = 1$ phases. The scale bars are 10 μm across in all images.

The lack of texture matches the poor morphology of these films and underscores that alternative approaches are required to induce preferential orientation in 2D/3D films with large nominal n values.

Contrary to the bulk of the film, a significant degree of orientation is already present, even in the pristine films when only the surface layer is probed. Although the addition of NH_4SCN further improves the texture, its presence appears to be less essential to inducing directional growth than it is in the bulk of the film. These results can be best understood in the recently proposed framework for the crystallization of 2D/3D perovskite films. In this model, the presence of large organic spacer cations in the precursor solution induces nucleation of a well-oriented layer of 3D-like perovskite phases at the liquid–air interface.[16,17,35] When the degree of supersaturation in the solution is low enough, the subsequent crystallization is templated by the surface layer such that a well-oriented film is obtained. If, on the other hand, supersaturation is high, bulk nucleation competes with uninterrupted crystal growth, and a randomly oriented film is obtained instead.[36] While the presence of PEA^+ is sufficient to induce a well-oriented surface layer in both the pristine and NH_4SCN films up to $\langle n \rangle = 5$, the addition of NH_4SCN is crucial to suppressing bulk nucleation and maintaining the orientation throughout the entire thickness of the 2D/3D film.

Confocal laser scanning microscopy (CLSM) was subsequently performed to investigate the spatial distribution of different perovskite phases within these films. The resulting photoluminescence (PL) maps are shown as RGB images in Figure 3, in which the red channel represents PL with an energy smaller than 1.91 eV corresponding to emission from the 3D or 3D-like perovskite phases, green corresponds to emitted photons with an energy between 1.94 and 2.30 eV corresponding to perovskite phases $n = 2$ and 3, and finally the blue channel contains all PL with an energy above 2.27 eV, which can be ascribed to the $n = 1$ phase. For reference, these ranges are also indicated in the average steady-state PL spectra of these films in Figure S13. From these PL maps, it is apparent that both $\langle n \rangle = 2$ films have a sizable contribution from low-dimensional perovskite phases, as expected from their respective steady-state PL spectra. Clear differences in the PL distribution between the two films can be seen for all channels. For the pristine film, the 3D-like emission follows the wrinkled pattern observed by AFM, with fine-grained emission from low-n-value phases superimposed. The PL map of the NH_4SCN films, on the other hand, shows a more segregated behavior, where PL from low-n-value phases stems from larger domains that have relatively little contribution from 3D-like phases. This suggests a larger degree of phase separation in the latter and closely matches the well-defined isolated crystallites observed by AFM.

Interestingly, despite the absence of clear signatures of low-n-value emission in the PL spectra for the $\langle n \rangle = 4$ films, both of these films also show emission in the green and blue channels, revealing the presence of intermediate- and low-n-value phases that are not detectable in the conventional steady-state PL measurements, where a spatial average of the PL is measured. As the nominal n value is further increased to 5, low-dimensional PL is no longer observable for the pristine film, and only small amounts are left for the NH_4SCN films. Finally, as expected from their steady-state spectra, the $\langle n \rangle = 20$ film cast with the additive again shows a large contribution from intermediate phases that are segregated from the 3D-like phases, whereas the pristine film shows no traces of PL from low-dimensional phases at all. The improvement in the texture and grain size of the 2D/3D films cast with NH_4SCN thus seems to come at the cost of increased surface roughness and phase separation of low-n-value perovskite phases.

Optical Properties. The mixture of different perovskite phases in 2D/3D films constitutes an inhomogeneous energetic landscape in which energy is typically found to funnel from high-band-gap to low-band-gap phases, from which an efficient radiative recombination of charge carriers then takes place.[37–40] Several reports have demonstrated the importance of crystallization dynamics by noting that the energetic landscape is sensitive to the choice of the organic spacer cation,[41–43] solvent,[44,45] and deposition process.[15] Even the stoichiometry of the precursor solution and variations in the ligand concentration across neighboring phases can change the photophysics of 2D/3D systems considerably.[46,47] More

https://doi.org/10.1021/acsaem.3c00545
ACS Appl. Energy Mater. 2023, 6, 10285–10293

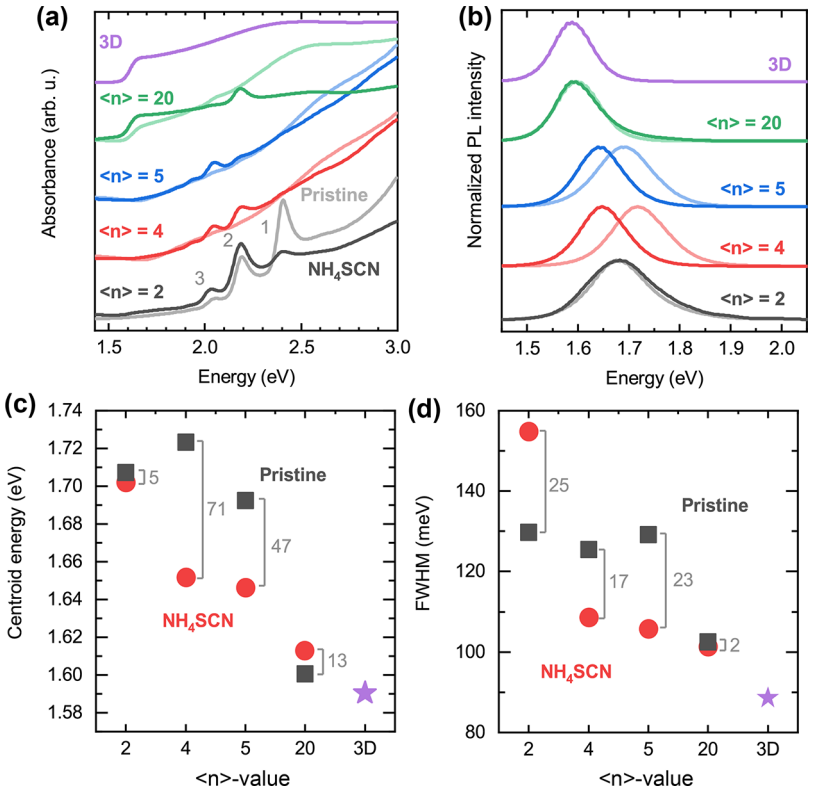

Figure 4. (a) Absorption and (b) PL spectra of the pristine film (shaded lines) compared to those of their NH_4SCN counterparts (dark lines) for different nominal n values. Nominal values of $\langle n \rangle$ = 2, 4, 5, and 20 are represented by gray, red, blue, and green lines, respectively, as indicated by the insets. The spectrum of a pristine 3D $MAPbI_3$ film is provided in purple as a reference. The gray insets in part a indicate the absorption peaks from perovskite phases of a specific n value. (c) Extracted centroid energy of the PL spectra in parts b and d of their full-width at half-maximum (FWHM) as a function of the nominal n value. The gray numbers in the inset denote absolute energy differences between the NH_4SCN and pristine films in units of millielectronvolts.

recently, some of us have reported that the addition of isopropylammonium to $(PEA)_2(Cs_{0.75}MA_{0.25})Pb_2Br_7$ is capable of blocking energy transfer to phases with $n > 3$ by changing the texture of the perovskite film.[48] Having established that the crystallization mechanism is strongly affected by the addition of NH_4SCN as well as the stoichiometry of the precursor solution, we then proceeded to investigate the optical properties of our films using absorption and PL spectroscopy.

The 3D and $\langle n \rangle$ = 20 films show a clear absorption onset corresponding to the band-gap energy of $MAPbI_3$ around 1.58 eV, indicating the dominance of 3D or 3D-like perovskite phases in these films (Figure 4a). For the lower $\langle n \rangle$ values, the sharp absorption onset from the 3D perovskite phase is suppressed to a large extent and is replaced by an absorption spectrum that steadily increases as a function of energy. Clear contributions from low-dimensional perovskite phases (n = 1–3, as indicated in the graph) can be observed in the absorption spectra, especially in the case of the $\langle n \rangle$ = 2 films (see Figure S14 for absolute absorption spectra). For the pristine films, low-dimensional absorption features lose in prominence as the amount of PEA decreases along the series $\langle n \rangle$ = 4, 5, and 20, for which they are only observable as minor modulations of the absorption line shape. In the case of films cast with NH_4SCN, however, low-dimensional perovskite absorption peaks remain clearly distinguishable even up to $\langle n \rangle$ = 20, confirming that a sizable number of low-dimensional perovskite phases reside within these films. Thus, the addition of ammonium thiocyanate to the precursor solution not only alters the film's texture and morphology but also significantly affects the phase distribution of 2D/3D perovskite films.

At this point, it should be noted that, upon excitation of the films from both their top surface and the perovskite/glass interface, it becomes apparent that in the NH_4SCN films the low-dimensional perovskite phases are accumulated at the substrate, conforming to a graded distribution that is typically observed in the 2D/3D film (Figure S15).[49] The pristine films, on the other hand, show minimal differences between the front and back surfaces of the film and no clear signs of emission from low-dimensional perovskite phases (with the exception of the extreme case of $\langle n \rangle$ = 2). The NH_4SCN films thus exhibit a much larger degree of phase separation along the thickness of the film. While their increased orientation increases the overall device performance, the presence of phase-separated low-dimensional perovskite phases at the bottom interface could pose a severe bottleneck for efficient charge transport throughout the active layer. Efforts should thus be directed toward striking a balance between increased orientation while minimizing large-scale phase separation when using NH_4SCN as an orientation-controlling additive in these systems. Another important observation to make here is that, for the $\langle n \rangle$ = 20 film cast with NH_4SCN, a less strong gradient is observed than those for the $\langle n \rangle$ = 4 and 5 films, with low-dimensional perovskites being pronounced both at the front and back sides of the film. This underscores the notion that the impact of NH_4SCN addition is different for the case in which only low quantities of PEA are present in the precursor solution.

https://doi.org/10.1021/acsaem.3c00545
ACS Appl. Energy Mater. 2023, 6, 10285–10293

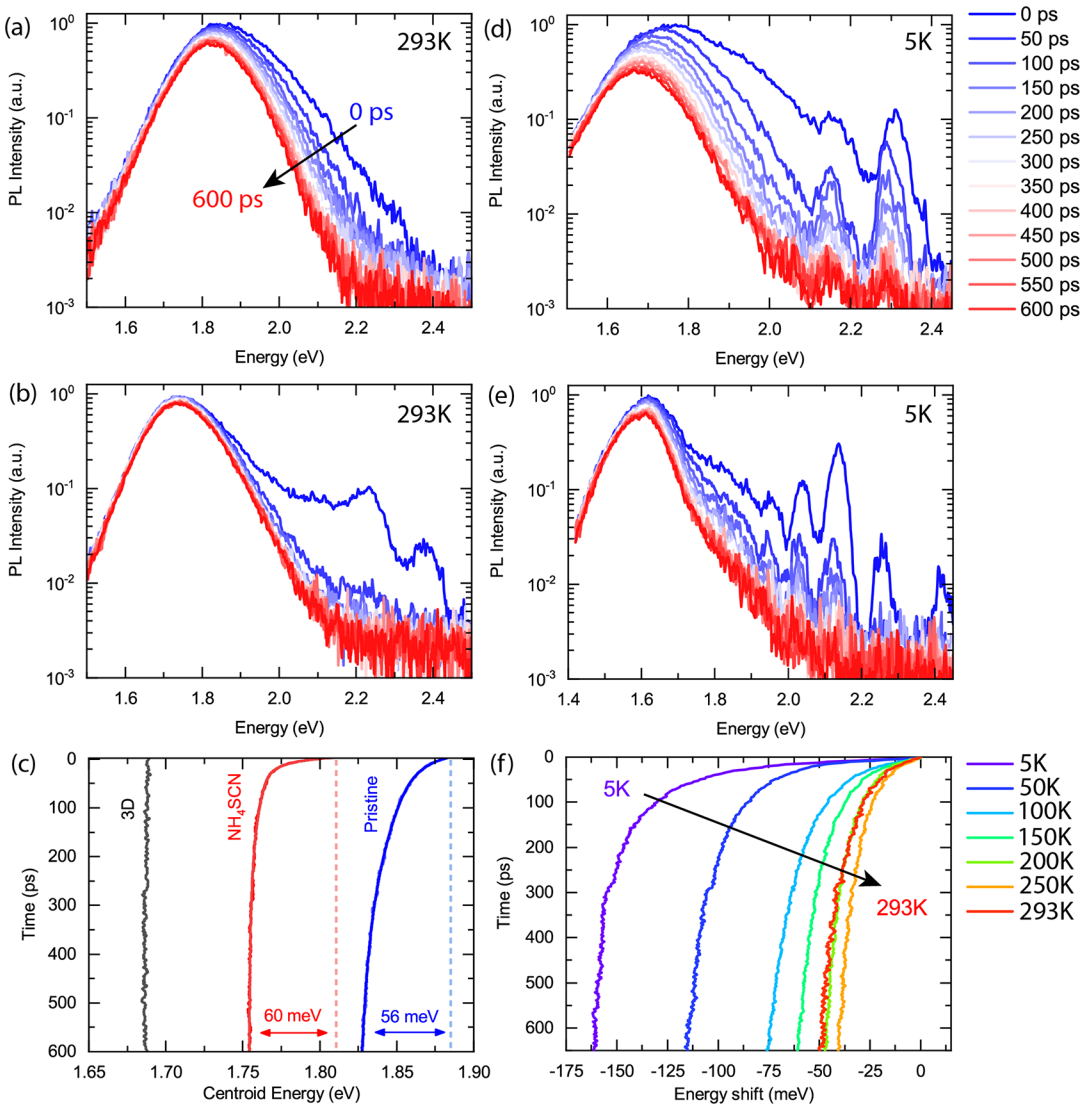

Figure 5. PL spectra at different times after excitation of the (a) pristine and (b) NH_4SCN $\langle n \rangle$ = 5 films at room temperature (293 K). The time interval between individual curves is 50 ps. (c) Centroid energy of emission from the same samples as a function of time after excitation. Time-dependent PL spectra of the (d) pristine and (e) NH_4SCN film as in parts a and b but measured at a temperature of 5 K. Note the different *x* scale for part e. (f) Extracted centroid energy as a function of the sample temperature for the pristine $\langle n \rangle$ = 5 film. All measurements were performed on the front surfaces of the perovskite films.

When considering the PL spectra measured from the front surface of the 2D/3D films, the PL spectra of the NH_4SCN films (Figure 4b) actually resemble more closely that of the 3D $MAPbI_3$ film than those of the pristine 2D/3D films. A pronounced red shift of the PL is observed upon the addition of NH_4SCN for the $\langle n \rangle$ = 4 and 5 films, bringing the centroid of the emission closer to that of the pristine 3D perovskite (Figure 4c). Accompanying this shift is a narrowing of the PL linewidth, which reflects a reduction in the energetic disorder of the 3D-like perovskite phases at the front surface of these films, as reported in Figure 4d. The reduced line width and emission energy both point to an efficient funnelling of energy toward low-band-gap phases or a reduced quantity of intermediate-to-high *n*-value phases in these samples, whereas in the pristine films, recombination takes place in a broader range of intermediate *n*-value phases.

Let us now take a closer look at the $\langle n \rangle$ = 5 films, which represent a composition that is most suitable for efficient solar cells, based on our previous experience with this material system.[15] In the case of the pristine film, the prompt PL consists of a single peak that exhibits an asymmetric tail extending toward higher energies, as displayed in Figure 5a. With increasing time after the initial photoexcitation, this high-energy tail diminishes as charge carriers recombine or are funneled down to the 3D-like phases through an energy cascade. The NH_4SCN film instead shows clear emission from the n = 2 and 1 perovskite phases that can be observed as distinct PL peaks in the prompt PL (Figure 5b). Within the first 50 ps after photoexcitation, these peaks have decayed entirely and virtually no low-dimensional PL is observable after that. As a result, both the pristine and NH_4SCN films show a time-dependent red shift due to the depopulation of high-energy states. While the magnitudes of this shift are similar (around 60 meV) in both cases, the red shift takes place within the first 100 ps for the NH_4SCN film but takes up to 500 ps for the pristine film (Figure 5c). Additionally, the centroid energy at which the emission stabilizes after the initial relaxation is considerably closer to the emission of $MAPbI_3$ at 1.69 eV for

https://doi.org/10.1021/acsaem.3c00545
ACS Appl. Energy Mater. 2023, 6, 10285−10293

the film cast with NH_4SCN (1.75 eV) than it is for the pristine film (1.83 eV).

Upon cooling of the sample to a temperature of 5 K, the emission from low-*n*-value perovskites becomes increasingly dominant for all samples (Figure S16), to such an extent that, even for the $\langle n \rangle$ = 5 films, the emission from low-dimensional phases is clearly observable. As can be seen from Figure 5d,e, the presence of low-*n*-value perovskite phases has a pronounced impact on the prompt PL at cryogenic temperatures. In the case of the pristine film, the rapid decay of the *n* = 1 and 2 phases is followed by a continuous red shift as the intermediate-*n*-value phases steadily decrease in intensity. Moreover, because the magnitude of this red shift decreases strongly with increasing temperature, it appears that the energy funneling in these 2D/3D films is a thermally activated process. This is further supported by the notion that the emission from the 3D-like perovskite phase in the $\langle n \rangle$ = 2 films shows a delayed onset at room temperature, indicating that repopulation of the 3D-like phases from low-*n*-value phases is taking place on a picosecond time scale (Figure S17). An initial decay in the emission intensity of the low-dimensional perovskite phases is observed to occur on similar time scales. This delayed onset similarly shows a strong temperature dependence and vanishes as the sample temperature is reduced and the funneling mechanism freezes out. In contrast to the continuous red shift observed for the pristine $\langle n \rangle$ = 5 film, the well-defined emission from low-*n*-value perovskite phases rapidly drops out for the NH_4SCN film and the emission is dominated by the 3D-like emission, which very closely matches the energy of the free exciton in the pure 3D perovskite (Figure S16).

The above details indicates that, despite the increased phase separation and prominence of low-dimensional phases in the NH_4SCN films, their high degree of ordering and crystallinity facilitates efficient energy transfer to 3D-like perovskite phases and gives rise to an energetic landscape that more closely resembles the pure 3D perovskite than the pristine 2D/3D perovskite films.

All in all, the impact of introducing ammonium thiocyanate into the precursor solution is not solely limited to improvement of the orientation and device performance of 2D/3D perovskites but also has major implications for the morphology, phase distribution, and energetic landscape of 2D/3D films. While at the front surface the NH_4SCN films are characterized by efficient energy funneling and a more 3D-like character than their pristine counterparts, the accumulation of low-dimensional perovskite at the bottom surface poses a potential bottleneck for the ultimate efficiency that can be achieved through this approach. The results presented in this work highlight that attempts to improve the quality of 2D/3D perovskites through adjustments in the deposition process should be carefully assessed in a framework extending beyond mere device performance to obtain a deeper understanding of the structure−property relationship in 2D/3D perovskite films.

CONCLUSION

The addition of orientation-controlling additives, such as thiocyanates, is a popular approach to increasing the efficiency of devices based on 2D/3D perovskite films. Here, the influence of NH_4SCN addition on the microstructural and optical properties of $(PEA)_2(MA)_{n-1}Pb_nI_{3n+1}$ was systematically investigated for different nominal values of *n*. The addition of NH_4SCN improves the orientation and crystallinity of the 3D-like perovskite phases as expected but also leads to an increased surface roughness and phase separation of low-dimensional perovskite phases in these samples. Nevertheless, the good crystallinity and efficient energy funneling in the NH_4SCN films make these materials attractive for their use as an active layer in solar cells, provided that phase separation is adequately controlled. The results presented in this work underline the complex energetic landscape of 2D/3D perovskite films and its sensitivity to processing conditions.

ASSOCIATED CONTENT

Supporting Information

The Supporting Information is available free of charge at https://pubs.acs.org/doi/10.1021/acsaem.3c00545.

Additional experimental details, materials, and methods, supplementary data including FTIR spectra of NH_4SCN-containing films, supplementary data and note 1 on X-ray characterization of all 2D/3D films described in this work, *J*−*V* curves of solar cells with $\langle n \rangle$ = 5, AFM micrographs of all films and their root-mean-square roughness values, raw and indexed GIWAXS data for pristine and NH_4SCN films and a 3D reference film, additional PL spectra of all films under front- and back-side excitation and their absorption spectra, and low-temperature PL spectra and time-resolved decay traces captured at different temperatures (PDF)

AUTHOR INFORMATION

Corresponding Author

Maria A. Loi − *Zernike Institute for Advanced Materials, University of Groningen, Groningen 9747 AG, The Netherlands*; orcid.org/0000-0002-7985-7431; Email: m.a.loi@rug.nl

Authors

Herman Duim − *Zernike Institute for Advanced Materials, University of Groningen, Groningen 9747 AG, The Netherlands*

Alex J. Rommens − *Zernike Institute for Advanced Materials, University of Groningen, Groningen 9747 AG, The Netherlands*

Shuyan Shao − *Zernike Institute for Advanced Materials, University of Groningen, Groningen 9747 AG, The Netherlands; Institute of Molecular Aggregation Science, Tianjin University, Tianjin 300072, China*

Giuseppe Portale − *Zernike Institute for Advanced Materials, University of Groningen, Groningen 9747 AG, The Netherlands*; orcid.org/0000-0002-4903-3159

Complete contact information is available at: https://pubs.acs.org/10.1021/acsaem.3c00545

Notes

The authors declare no competing financial interest.

ACKNOWLEDGMENTS

The authors express their gratitude to A. F. Kamp and T. Zaharia for their technical support. E. K. Tekelenburg and G. R. Blake are acknowledged for valuable discussion in the preparation of this manuscript. This work is part of the research program of the Foundation for Fundamental Research on Matter (FOM), which is part of The Netherlands Organization for Scientific Research. This is a publication of

the FOM-focus Group "Next Generation Organic Photovoltaics", participating in the Dutch Institute for Fundamental Energy Research.

REFERENCES

(1) Kim, J. Y.; Lee, J.-W.; Jung, H. S.; Shin, H.; Park, N.-G. High-Efficiency Perovskite Solar Cells. *Chem. Rev.* **2020**, *120*, 7867−7918.
(2) Quan, L. N.; Garcia de Arquer, F. P.; Sabatini, R. P.; Sargent, E. H. Perovskites for Light Emission. *Adv. Mater.* **2018**, *30*, 1801996.
(3) Li, C.; Wang, H.; Wang, F.; Li, T.; Xu, M.; Wang, H.; Wang, Z.; Zhan, X.; Hu, W.; Shen, L. Ultrafast and Broadband Photodetectors Based on a Perovskite/Organic Bulk Heterojunction for Large-Dynamic-Range Imaging. *Light Sci. Appl.* **2020**, *9*, 1−8.
(4) Wu, H.; Ge, Y.; Niu, G.; Tang, J. Metal Halide Perovskites for X-Ray Detection and Imaging. *Matter* **2021**, *4*, 144−163.
(5) Liao, K.; Hu, X.; Cheng, Y.; Yu, Z.; Xue, Y.; Chen, Y.; Gong, Q. Spintronics of Hybrid Organic−Inorganic Perovskites: Miraculous Basis of Integrated Optoelectronic Devices. *Adv. Opt. Mater.* **2019**, *7*, 1900350.
(6) Jeong, J.; Kim, M.; Seo, J.; Lu, H.; Ahlawat, P.; Mishra, A.; Yang, Y.; Hope, M. A.; Eickemeyer, F. T.; Kim, M.; Yoon, Y. J.; Choi, I. W.; Darwich, B. P.; Choi, S. J.; Jo, Y.; Lee, J. H.; Walker, B.; Zakeeruddin, S. M.; Emsley, L.; Rothlisberger, U.; Hagfeldt, A.; Kim, D. S.; Grätzel, M.; Kim, J. Y. Pseudo-Halide Anion Engineering for α-$FAPbI_3$ Perovskite Solar Cells. *Nature* **2021**, *592*, 381−385.
(7) Deretzis, I.; Smecca, E.; Mannino, G.; La Magna, A.; Miyasaka, T.; Alberti, A. Stability and Degradation in Hybrid Perovskites: Is the Glass Half-Empty or Half-Full? *J. Phys. Chem. Lett.* **2018**, *9*, 3000−3007.
(8) Wali, Q.; Iftikhar, F. J.; Khan, M. E.; Ullah, A.; Iqbal, Y.; Jose, R. Advances in Stability of Perovskite Solar Cells. *Org. Electron.* **2020**, *78*, 105590.
(9) Li, M.; Li, H.; Fu, J.; Liang, T.; Ma, W. Recent Progress on the Stability of Perovskite Solar Cells in a Humid Environment. *J. Phys. Chem. C* **2020**, *124*, 27251−27266.
(10) Soe, C. M. M.; Nagabhushana, G. P.; Shivaramaiah, R.; Tsai, H.; Nie, W.; Blancon, J.-C.; Melkonyan, F.; Cao, D. H.; Traoré, B.; Pedesseau, L.; Kepenekian, M.; Katan, C.; Even, J.; Marks, T. J.; Navrotsky, A.; Mohite, A. D.; Stoumpos, C. C.; Kanatzidis, M. G. Structural and Thermodynamic Limits of Layer Thickness in 2D Halide Perovskites. *Proc. Natl. Acad. Sci. U. S. A.* **2019**, *116*, 58−66.
(11) Yang, Y.; Gao, F.; Gao, S.; Wei, S.-H. Origin of the Stability of Two-Dimensional Perovskites: A First-Principles Study. *J. Mater. Chem. A* **2018**, *6*, 14949−14955.
(12) Blancon, J.-C.; Stier, A. V.; Tsai, H.; Nie, W.; Stoumpos, C. C.; Traoré, B.; Pedesseau, L.; Kepenekian, M.; Katsutani, F.; Noe, G. T.; Kono, J.; Tretiak, S.; Crooker, S. A.; Katan, C.; Kanatzidis, M. G.; Crochet, J. J.; Even, J.; Mohite, A. D. Scaling Law for Excitons in 2D Perovskite Quantum Wells. *Nat. Commun.* **2018**, *9*, 1−10.
(13) Zhang, F.; Lu, H.; Tong, J.; Berry, J. J.; Beard, M. C.; Zhu, K. Advances in Two-Dimensional Organic-Inorganic Hybrid Perovskites. *Energy Environ. Sci.* **2020**, *13*, 1154−1186.
(14) Grancini, G.; Nazeeruddin, M. K. Dimensional Tailoring of Hybrid Perovskites for Photovoltaics. *Nat. Rev. Mater.* **2019**, *4*, 4−22.
(15) Shao, S.; Duim, H.; Wang, Q.; Xu, B.; Dong, J.; Adjokatse, S.; Blake, G. R.; Protesescu, L.; Portale, G.; Hou, J.; Saba, M.; Loi, M. A. Tuning the Energetic Landscape of Ruddlesden−Popper Perovskite Films for Efficient Solar Cells. *ACS Energy Lett.* **2020**, *5*, 39−46.
(16) Zhang, J.; Zhang, L.; Li, X.; Zhu, X.; Yu, J.; Fan, K. Binary Solvent Engineering for High-Performance Two-Dimensional Perovskite Solar Cells. *ACS Sustain. Chem. Eng.* **2019**, *7*, 3487−3495.
(17) Chen, A. Z.; Shiu, M.; Ma, J. H.; Alpert, M. R.; Zhang, D.; Foley, B. J.; Smilgies, D.-M.; Lee, S.-H.; Choi, J. J. Origin of Vertical Orientation in Two-Dimensional Metal Halide Perovskites and its Effect on Photovoltaic Performance. *Nat. Commun.* **2018**, *9*, 1−7.
(18) Tsai, H.; Nie, W.; Blancon, J. C.; Stoumpos, C. C.; Asadpour, R.; Harutyunyan, B.; Neukirch, A. J.; Verduzco, R.; Crochet, J. J.; Tretiak, S.; Pedesseau, L.; Even, J.; Alam, M. A.; Gupta, G.; Lou, J.; Ajayan, P. M.; Bedzyk, M. J.; Kanatzidis, M. G.; Mohite, A. D. High-Efficiency Two-Dimensional Ruddlesden-Popper Perovskite Solar Cells. *Nature* **2016**, *536*, 312−317.
(19) Tsai, H.; Nie, W.; Blancon, J. C.; Stoumpos, C. C.; Soe, C. M. M.; Yoo, J.; Crochet, J.; Tretiak, S.; Even, J.; Sadhanala, A.; Azzellino, G.; Brenes, R.; Ajayan, P. M.; Bulović, V.; Stranks, S. D.; Friend, R. H.; Kanatzidis, M. G.; Mohite, A. D. Stable Light-Emitting Diodes Using Phase-Pure Ruddlesden−Popper Layered Perovskites. *Adv. Mater.* **2018**, *30*, 1704217.
(20) Tai, Q.; You, P.; Sang, H.; Liu, Z.; Hu, C.; Chan, H. L.; Yan, F. Efficient and Stable Perovskite Solar Cells Prepared in Ambient Air Irrespective of the Humidity. *Nat. Commun.* **2016**, *7*, 1−8.
(21) Tang, G.; Yang, C.; Stroppa, A.; Fang, D.; Hong, J. Revealing the Role of Thiocyanate Anion in Layered Hybrid Halide Perovskite $(CH_3NH_3)_2Pb(SCN)_2I_2$. *J. Chem. Phys.* **2017**, *146*, 224702.
(22) Chen, Y.; Li, B.; Huang, W.; Gao, D.; Liang, Z. Efficient and Reproducible $CH_3NH_3PbI_{3-x}(SCN)_x$ Perovskite Based Planar Solar Cells. *Chem. Commun.* **2015**, *51*, 11997−11999.
(23) Jiang, Q.; Rebollar, D.; Gong, J.; Piacentino, E. L.; Zheng, C.; Xu, T. Pseudohalide-Induced Moisture Tolerance in Perovskite $CH_3NH_3Pb(SCN)_2I$ Thin Films. *Angew. Chem., Int. Ed.* **2015**, *54*, 7617−7620.
(24) Ke, W.; Xiao, C.; Wang, C.; Saparov, B.; Duan, H. S.; Zhao, D.; Xiao, Z.; Schulz, P.; Harvey, S. P.; Liao, W.; Meng, W.; Yu, Y.; Cimaroli, A. J.; Jiang, C. S.; Zhu, K.; Al-Jassim, M.; Fang, G.; Mitzi, D. B.; Yan, Y. Employing Lead Thiocyanate Additive to Reduce the Hysteresis and Boost the Fill Factor of Planar Perovskite Solar Cells. *Adv. Mater.* **2016**, *28*, 5214−5221.
(25) Yang, S.; Liu, W.; Zuo, L.; Zhang, X.; Ye, T.; Chen, J.; Li, C. Z.; Wu, G.; Chen, H. Thiocyanate Assisted Performance Enhancement of Formamidinium Based Planar Perovskite Solar Cells Through a Single One-Step Solution Process. *J. Mater. Chem. A* **2016**, *4*, 9430−9436.
(26) Yu, Y.; Wang, C.; Grice, C. R.; Shrestha, N.; Chen, J.; Zhao, D.; Liao, W.; Cimaroli, A. J.; Roland, P. J.; Ellingson, R. J.; Yan, Y. Improving the Performance of Formamidinium and Cesium Lead Triiodide Perovskite Solar Cells using Lead Thiocyanate Additives. *ChemSusChem* **2016**, *9*, 3288−3297.
(27) Chiang, Y. H.; Li, M. H.; Cheng, H. M.; Shen, P. S.; Chen, P. Mixed Cation Thiocyanate-Based Pseudohalide Perovskite Solar Cells With High Efficiency and Stability. *ACS Appl. Mater. Interfaces* **2017**, *9*, 2403−2409.
(28) Yi, H.; Duan, L.; Haque, F.; Bing, J.; Zheng, J.; Yang, Y.; Mo, A. C.; Zhang, Y.; Xu, C.; Conibeer, G.; Uddin, A. Thiocyanate Assisted Nucleation For High Performance Mix-Cation Perovskite Solar Cells with Improved Stability. *J. Power Sources* **2020**, *466*, 228320.
(29) Zhang, X.; Wu, G.; Yang, S.; Fu, W.; Zhang, Z.; Chen, C.; Liu, W.; Yan, J.; Yang, W.; Chen, H. Vertically Oriented 2D Layered Perovskite Solar Cells with Enhanced Efficiency and Good Stability. *Small* **2017**, *13*, 1700611.
(30) Zhang, X.; Wu, G.; Fu, W.; Qin, M.; Yang, W.; Yan, J.; Zhang, Z.; Lu, X.; Chen, H. Orientation Regulation of Phenylethylammonium Cation Based 2D Perovskite Solar Cell with Efficiency Higher Than 11. *Adv. Energy Mater.* **2018**, *8*, 1702498.
(31) Li, F.; Zhang, J.; Jo, S. B.; Qin, M.; Li, Z.; Liu, T.; Lu, X.; Zhu, Z.; Jen, A. K. Vertical Orientated Dion−Jacobson Quasi-2D Perovskite Film with Improved Photovoltaic Performance and Stability. *Small Methods* **2020**, *4*, 1900831.
(32) Ruggeri, E.; Anaya, M.; Gałkowski, K.; Delport, G.; Kosasih, F. U.; Abfalterer, A.; Mackowski, S.; Ducati, C.; Stranks, S. D. Controlling the Growth Kinetics and Optoelectronic Properties of 2D/3D Lead−Tin Perovskite Heterojunctions. *Adv. Mater.* **2019**, *31*, 1905247.
(33) Song, T.-B.; Yuan, Z.; Mori, M.; Motiwala, F.; Segev, G.; Masquelier, E.; Stan, C. V.; Slack, J. L.; Tamura, N.; Sutter-Fella, C. M. Revealing the Dynamics of Hybrid Metal Halide Perovskite Formation via Multimodal In Situ Probes. *Adv. Funct. Mater.* **2020**, *30*, 1908337.

https://doi.org/10.1021/acsaem.3c00545
ACS Appl. Energy Mater. 2023, 6, 10285−10293

(34) Duim, H.; ten Brink, G. H.; Adjokatse, S.; de Kloe, R.; Kooi, B. J.; Portale, G.; Loi, M. A. Unraveling the Microstructure of Layered Metal Halide Perovskite Films. *Small Struct* **2020**, *1*, 2000074.
(35) Dong, J.; Shao, S.; Kahmann, S.; Rommens, A. J.; Hermida-Merino, D.; ten Brink, G. H.; Loi, M. A.; Portale, G. Mechanism of Crystal Formation in Ruddlesden−Popper Sn-Based Perovskites. *Adv. Funct. Mater.* **2020**, *30*, 2001294.
(36) Chen, A. Z.; Shiu, M.; Deng, X.; Mahmoud, M.; Zhang, D.; Foley, B. J.; Lee, S.-H.; Giri, G.; Choi, J. J. Understanding the Formation of Vertical Orientation in Two-dimensional Metal Halide Perovskite Thin Films. *Chem. Mater.* **2019**, *31*, 1336−1343.
(37) Yuan, M.; Quan, L. N.; Comin, R.; Walters, G.; Sabatini, R.; Voznyy, O.; Hoogland, S.; Zhao, Y.; Beauregard, E. M.; Kanjanaboos, P.; Lu, Z.; Kim, D. H.; Sargent, E. H. Perovskite Energy Funnels for Efficient Light-Emitting Diodes. *Nat. Nanotechnol.* **2016**, *11*, 872−877.
(38) Jiang, Y.; Wei, J.; Yuan, M. Energy-Funneling Process in Quasi-2D Perovskite Light-Emitting Diodes. *J. Phys. Chem. Lett.* **2021**, *12*, 2593−2606.
(39) Proppe, A. H.; Elkins, M. H.; Voznyy, O.; Pensack, R. D.; Zapata, F.; Besteiro, L. V.; Quan, L. N.; Quintero-Bermudez, R.; Todorovic, P.; Kelley, S. O.; Govorov, A. O.; Gray, S. K.; Infante, I.; Sargent, E. H.; Scholes, G. D. Spectrally Resolved Ultrafast Exciton Transfer in Mixed Perovskite Quantum Wells. *J. Phys. Chem. Lett.* **2019**, *10*, 419−426.
(40) Williams, O. F.; Guo, Z.; Hu, J.; Yan, L.; You, W.; Moran, A. M. Energy Transfer Mechanisms in Layered 2D Perovskites. *J. Chem. Phys.* **2018**, *148*, 134706.
(41) Panuganti, S.; Besteiro, L. V.; Vasileiadou, E. S.; Hoffman, J. M.; Govorov, A. O.; Gray, S. K.; Kanatzidis, M. G.; Schaller, R. D. Distance Dependence of Förster Resonance Energy Transfer Rates in 2D Perovskite Quantum Wells via Control of Organic Spacer Length. *J. Am. Chem. Soc.* **2021**, *143*, 4244−4252.
(42) Zheng, K.; Chen, Y.; Sun, Y.; Chen, J.; Chábera, P.; Schaller, R.; Al-Marri, M. J.; Canton, S. E.; Liang, Z.; Pullerits, T. Inter-Phase Charge and Energy Transfer in Ruddlesden−Popper 2D Perovskites: Critical Role of the Spacing Cations. *J. Mater. Chem. A* **2018**, *6*, 6244−6250.
(43) Proppe, A. H.; Quintero-Bermudez, R.; Tan, H.; Voznyy, O.; Kelley, S. O.; Sargent, E. H. Synthetic Control over Quantum Well Width Distribution and Carrier Migration in Low-Dimensional Perovskite Photovoltaics. *J. Am. Chem. Soc.* **2018**, *140*, 2890−2896.
(44) Cao, D. H.; Stoumpos, C. C.; Yokoyama, T.; Logsdon, J. L.; Song, T.-B.; Farha, O. K.; Wasielewski, M. R.; Hupp, J. T.; Kanatzidis, M. G. Thin Films and Solar Cells Based on Semiconducting Two-Dimensional Ruddlesden−Popper $(CH_3(CH_2)_3NH_3)_2(CH3NH3)_{n-1}Sn_nI_{3n+1}$ Perovskites. *ACS Energy Lett.* **2017**, *2*, 982−990.
(45) Bruening, K.; Tassone, C. J. Antisolvent Processing of Lead Halide Perovskite Thin Films Studied by In Situ X-ray Diffraction. *J. Mater. Chem. A* **2018**, *6*, 18865−18870.
(46) Shao, S.; Nijenhuis, M.; Dong, J.; Kahmann, S.; ten Brink, G. H.; Portale, G.; Loi, M. A. Influence of the Stoichiometry of Tin-Based 2D/3D Perovskite Active Layers on Solar Cell Performance. *J. Mater. Chem. A* **2021**, *9*, 10095−10103.
(47) Quintero-Bermudez, R.; Proppe, A. H.; Mahata, A.; Todorovic, P.; Kelley, S. O.; De Angelis, F.; Sargent, E. H. Ligand-Induced Surface Charge Density Modulation Generates Local Type-II Band Alignment in Reduced-Dimensional Perovskites. *J. Am. Chem. Soc.* **2019**, *141*, 13459−13467.
(48) Rivera Medina, M. J.; Di Mario, L.; Kahmann, S.; Xi, J.; Portale, G.; Bongiovanni, G.; Mura, A.; Alonso Huitrón, J. C.; Loi, M. A. Tuning the energy transfer in Ruddlesden−Popper perovskites phases through isopropylammonium addition − towards efficient blue emitters. *Nanoscale* **2023**, *15*, 6673−6685.
(49) Liu, N.; Liu, P.; Ren, H.; Xie, H.; Zhou, N.; Gao, Y.; Li, Y.; Zhou, H.; Bai, Y.; Chen, Q. Probing Phase Distribution in 2D Perovskites for Efficient Device Design. *ACS Appl. Mater. Interfaces* **2020**, *12*, 3127−3133.

https://doi.org/10.1021/acsaem.3c00545
ACS Appl. Energy Mater. 2023, 6, 10285−10293